Journal of Photochemistry & Photobiology, B: Biology 245 (2023) 112754

Contents lists available at ScienceDirect

Journal of Photochemistry & Photobiology, B: Biology

journal homepage: www.elsevier.com/locate/jphotobiol

Dynamic photodamage of red blood cell induced by CisDiMPyP porphyrin

Gustavo Scanavachi [a,b,1], Koji Kinoshita [a,c,d,*,1], Tayana M. Tsubone [a,e], Rosangela Itri [a,*]

[a] Institute of Physics, University of São Paulo, São Paulo, Brazil
[b] Department of Cell Biology, Harvard Medical School, Program in Cellular and Molecular Medicine (PCMM), Boston Children's Hospital, Boston, MA 02115, United States
[c] Department of Molecular Medicine, University of Southern Denmark, Odense, Denmark
[d] Department of Biological Chemistry and Molecular Pharmacology (BCMP), Harvard Medical School, Program in Cellular and Molecular Medicine (PCMM), Boston Children's Hospital, Boston, MA 02115, United States
[e] Institute of Chemistry, Federal University of Uberlandia, Minas Gerais, Brazil

A B S T R A C T

It is well-known that oxidative damage in red blood cell (RBC) usually causes morphological changes and increased membrane rigidity. Although many studies have focused on investigating how RBC responds to a photodynamic stimulus, the intermediate steps between membrane damage and hemolysis are not reported. To give a comprehensive insight into changes of RBC membrane property under different oxidative damage levels, we employed the photoactivation of CisDiMPyP porphyrin that primarily generates singlet oxygen $^1O_2$ as oxidant species. We found that there were distinguishable characteristic damages depending on the $^1O_2$ flux over the membrane, in a way that each impact of photooxidative damage was categorized under three damage levels: mild (maintaining the membrane morphology and elasticity), moderate (membrane elongation and increased membrane elasticity) and severe (wrinkle-like deformation and hemolysis). When sodium azide (NaN_3) was used as a singlet oxygen quencher, delayed cell membrane alterations and hemolysis were detected. The delay times showed that $^1O_2$ indeed plays a key role that causes RBC photooxidation by CisDiMPyP. We suggest that the sequence of morphological changes (RBC discoid area expansion, wrinkle-like patterns, and hemolysis) under photooxidative damage occurs due to damage to the lipid membrane and cytoskeletal network proteins.

1. Introduction

Red blood cell (RBC or erythrocyte) is the most abundant cell in the human body representing around 84% of the total cells [1]. Deformability is a crucial characteristic that allows RBC to pass through narrow capillaries thus carrying/delivering oxygen and removing carbon dioxide across the whole human body [2]. It has been previously reported that oxidative stress may induce RBC's morphological alterations (deformation and/or rupture) as well as changes in membrane rigidity. However, the damage to RBC depends on the oxidative species and the level of oxidative stress [3–5].

Studies focusing on RBC oxidative damage being promoted by photodynamic action, have shown membrane hemolysis in the presence of photoactivated photosensitizers [5,6]. It is well known that reactive oxygen species, such as superoxide ions ($O_2^{\bullet-}$), hydrogen peroxide (H_2O_2), hydroxyl radical ($HO^{\bullet}$), and singlet oxygen ($^1O_2$) can be produced by a photosensitizer in the presence of light and oxygen [7,8]. In particular, $^1O_2$ can damage various components of cell membranes, such as amino acids [9,10], unsaturated fatty acids [7,11,12], and cholesterol [13,14]. Sonoda et al. showed a significant contribution of $^1O_2$ in RBC photohemolysis [6] which was delayed in the presence of tryptophan, a scavenger of $^1O_2$, while the presence of mannitol and glycerol, scavengers mainly of OH radicals, does not prevent the RBC leakage to the same extent [6]. In agreement with the main role of $^1O_2$ in photohemolysis, Girotti's group provides unambiguous evidence for large-scale $^1O_2$ intermediacy during photodamage of ghost erythrocytes, after the identification of 3β-hydroxy-5α-cholest-6-ene-5-hydroperoxide (5α -OOH) as a major photoproduct of lipid peroxidation in a model membrane [15,16].

Several reports in the 1980s described that photosensitization might form covalent cross-linking between polypeptides via SH-groups, NH_2-groups, histidine-groups, carbonylation, spectrin-hemoglobin complex, and hemoglobin aggregation [17–24]. RBC photodamage caused either by lipid peroxidation or by protein cross-linking (or both), undoubtedly may contribute to changes in erythrocyte deformability [25].

Although several studies have focused on understanding how RBC responds to a photodynamic stimulus, there is a gap in understanding of the steps of membrane damage induced by photooxidation and the sequence of events that leads to hemolysis, mediated by increased membrane stiffness caused by the cytoskeleton. In this regard, this work

* Corresponding authors at: Institute of Physics, University of São Paulo, São Paulo, Brazil.
E-mail addresses: Koji.Kinoshita@childrens.harvard.edu (K. Kinoshita), itri@if.usp.br (R. Itri).
[1] These authors contributed equally to this work.

https://doi.org/10.1016/j.jphotobiol.2023.112754
Received 12 March 2023; Received in revised form 18 June 2023; Accepted 2 July 2023
Available online 3 July 2023

aims to fill this gap by photooxidizing RBC in a controlled manner. To this end, a cationic porphyrin-based photosensitizer, meso-cis-di (*N*-methyl-4-pyridyl) diphenyl porphyrin dichloride (CisDiMPyP), that partitions preferentially into the RBC membrane [5], was used as singlet oxygen generator to trigger the RBC photooxidation. The CisDiMPyP quantum yield value of singlet oxygen is 0.74 and its quantum yield value of fluorescence is 0.11, which means that absorption of each photon results in 74% singlet oxygen generation and 11% fluorescence [5]. The other 15% are divided into several possibilities of photophysics processes, i.e. internal conversion, phosphorescence, and/or Type I reactions. Thus, CisDiMPyP generates mostly singlet oxygen through Type II reactions. [26,27].

Controlling CisDiMPyP concentration, and in turn the singlet oxygen production rate, allows us to follow the RBC morphological changes depending on the photooxidative damage level associated with membrane area increase coupled to shear modulus increase and appearance of membrane wrinkles until hemolysis takes place.

2. Materials and Methods

2.1. Materials

Meso-cis-di (*N*-methyl-4-pyridyl) diphenyl porphyrin dichloride (CisDiMPyP) was purchased from Frontier Scientific (Logan, UT). Sodium chloride (NaCl) was acquired from VWR International (Radnor, PA). Buffer, sodium azide (99%), bovine serum albumin (BSA), and any other common reagents were purchased from Sigma-Aldrich (St. Louis, MO).

2.2. Donors of RBC Samples

Following the cooperation agreement on blood for research or quality assurance (Project number DP059, Application for blood for research or quality assurance, Document-620.8, South Danish Transfusion Service and Tissue Centre, Department of Clinical Immunology, Odense University Hospital (Denmark)), healthy donors' human blood was collected in vacutainer blood collection tubes (stock RBC sample) containing EDTA to avoid coagulation. This study was approved by the ethical committee of Odense University Hospital and by the University of Southern Denmark (SDU).

2.3. Sample Preparation

For each experiment, an aliquot of RBC suspension was washed three times with 20 mM phosphate buffer saline (PBS), pH 7.4, containing 150 mM NaCl (~300 mOsm), by centrifugation at 500*g* for 3 min at 20 °C. The washed RBCs were then suspended in the PBS buffer containing 0.1% BSA and used on the same day. The RBC suspension in each vacutainer blood collection tube was stocked for up to 2 days in the refrigerator.

A stock solution of CisDiMPyP (> 100 μM) was prepared in 5 mM Tris-HCl buffer (pH 7.4) and diluted to 50–5000 nM depending on the experiment purpose (morphological/hemolysis tests, and membrane elasticity measurements – see ahead in the text). CisDiMPyP concentration was determined by the absorption value at wavelength $\lambda = 422$ nm (molar extinction coefficient $\varepsilon = 171 \times 10^3\ M^{-1}\ cm^{-1}$ in methanol [5]) with a Shimazu UV-2600 spectrophotometer. To obtain the equilibrium of the CisDiMPyP adsorption at the RBC membrane, the porphyrin was added to each RBC sample (hematocrit: ~ 0.01% in volume) with a continuous shake in the dark for 20 min before the experiments [5]. The photooxidative damage depends on the photosensitizer concentration, the power of light irradiation, and the irradiation time. As the CisDiMPyP has a high quantum yield of $^1O_2$ generation (0.74 in methanol), we shall here consider that the photooxidative damage at RBC membrane is mainly caused by $^1O_2$ formation upon CisDiMPyP photoactivation [5,28]. The singlet oxygen $^1O_2$ production rate, Q, in/near the RBC membrane surface can be calculated according to eq. 1 (see Section 2.4). All experiments were performed at room temperature (~20 °C).

For the RBC membrane shear modulus measurement, RBCs were further washed five times to remove the photosensitizer from the erythrocyte membrane surface after each irradiation by using the centrifugation washing process (500 *g* for 3 min at 20 °C). The washing step was essential to maintain the photooxidative damage level constant during the shear modulus measurement (no elasticity recovery during the process). This is because the micropipette aspiration technique requires continuous irradiation to watch the image with the camera during the measurement (irradiance: 26 J/m^2s at 546 nm, see Section 2.4).

It is important to mention that three different controls were done: i) porphyrin-free RBC assays without irradiation; ii) porphyrin-free RBC assays under 546 ± 10 nm light irradiation; iii) RBC assays containing porphyrin without light irradiation. These controls did not exert any RBC morphological alterations and/or cell membrane disruption. Therefore, they are not presented unless mentioned in the text.

2.4. In Situ Irradiation

Fig. 1A presents the absorption (blue line) and fluorescence (red line) spectra from CisDiMPyP, where one can observe a strong absorption peak at 430 nm and a small absorption peak at around 530 nm.

In Fig. 1B, the homogeneous partition of the photosensitizer in the RBC membrane was visualized by confocal microscopy with excitation at $\lambda_{exc} = 543$ nm using a HeNe Laser and fluorescence observed at $\lambda_{em} >$ 560 nm (Fig. 1A).

To observe the RBC morphological changes during the in-situ irradiation, a bright-field microscope, an Axiovert inverted microscope (Carl Zeiss Microimaging, Inc., Thornwood, NY), with a custom-built magnifying lens was used. All images were taken using the 40× magnification air objective lens (NA 0.75). With the aim to better visualize the RBC morphological changes due to photooxidation (bigger magnification), 16× eyepiece lens from Carl Zeiss Microimaging was adapted at the front of the CCD camera (30 frames/s, DAGE-MIT, IN) with the microscope setup.

The irradiation was performed using a bandpass filter of 546 nm ± 10 nm attached to the microscope beam path. Using the spectrometer StellarNet EPP2000C-25 μm (StellarNet Inc., FL), the irradiance E_e of the beamline was detected at the specimen focal plane. Fig. 2A presents the halogen lamp irradiance profile measured for each used condition in the pre-irradiation and irradiation set-up. Accordingly, the irradiance peak values of low and high power of the halogen lamp amounted to $E_e =$ 0.28 J/m^2 s and 26 J/m^2 s at 546 nm, respectively. These two different irradiances were used depending on the purpose: low irradiance E_e to find and focus RBCs at the focal plane in the microscope's field of view (about a few seconds); and high irradiance E_e in the photosensitization procedure.

For quantitative analysis, the singlet oxygen $^1O_2$ production rate (Q) was calculated at the wavelength $\lambda = 546$ nm, knowing the irradiance E_e [29]:

$$Q(C_p) = \frac{\Phi_p C_p \lambda E_e \sigma}{hc} \quad (1)$$

where Φ_p is the CisDiMPyP $^1O_2$ generation quantum yield, $\Phi_p = 0.74$ [5], C_p is the photosensitizer concentration, σ is the CisDiMPyP molar absorbance cross section, *h* is the Planck constant and *c* is the light speed. C_p was determined by the absorption experiment results (Fig. 1) [5]. σ was calculated considering $\sigma(\lambda) = 3.82\ x\ 10^{-21}\ \varepsilon(\lambda)$ [30], where ε (546 nm) $= 10 \times 10^3\ (M{\cdot}cm)^{-1}$ is the wavelength dependent-molar extinction coefficient of porphyrin [5].

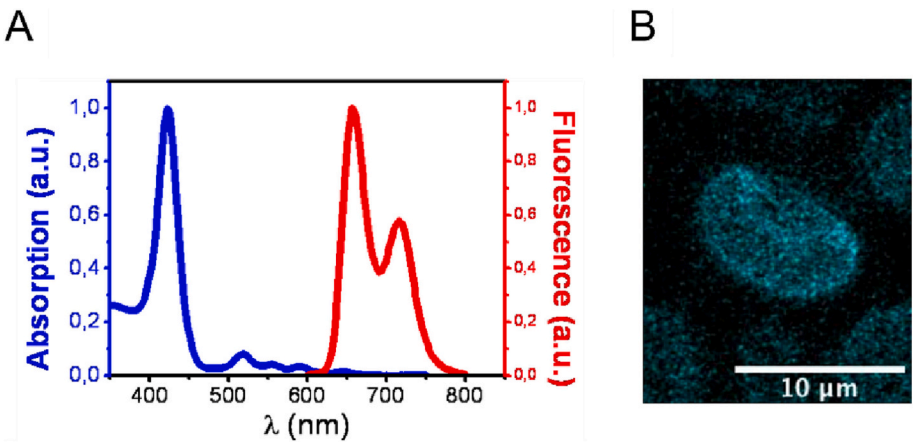

Fig. 1. (A) Normalized CisDiMPyP absorption and fluorescence spectra (B) Distribution of CisDiMPyP (500 nM) at the RBC surface measured by confocal microscopy ($\lambda_{exc} = 543$ nm, $\lambda_{em} > 560$ nm).

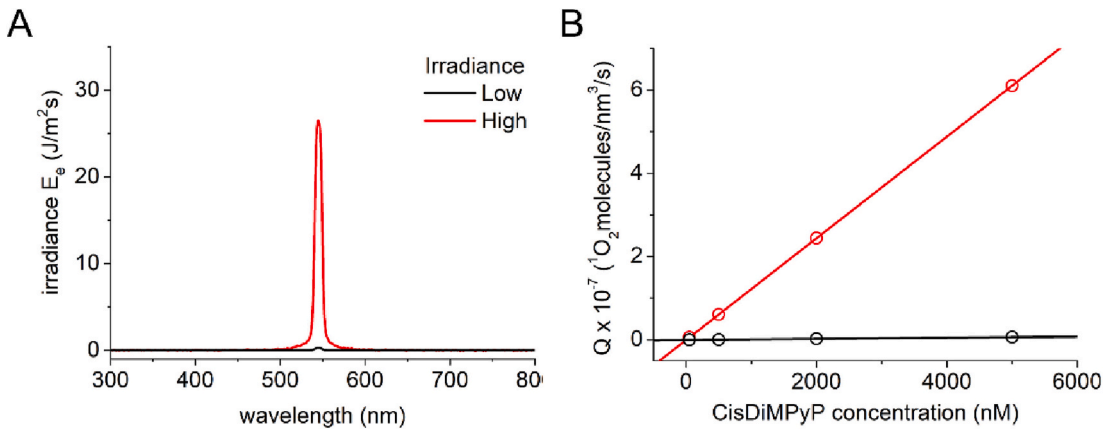

Fig. 2. Halogen lamp irradiance and the singlet oxygen $^1O_2$ production rate Q. (A) Halogen lamp irradiance profile in the wavelength region between 300 and 800 nm. The halogen light wavelength was controlled by a green bandpass filter (546 ± 10 nm) (see Supporting Information, Fig. S1). The black and red solid lines show each low and high irradiance E_e, which is controlled by the low and high power of the light. (B) Calculated singlet oxygen $^1O_2$ production rate Q of low and high irradiance E_e for each CisDiMPyP concentration by using the relationship in eq. 1. The highlighted Q values with open symbols correspond to 50, 500, 2000, and 5000 nM CisDiPyP concentrations, which were used for the experiments. (For interpretation of the references to colour in this figure legend, the reader is referred to the web version of this article.)

2.5. *Micropipette Aspiration Technique and Shear Modulus Data Analysis*

The micropipette aspiration technique has been well established as a device to measure the RBC membrane's mechanical property or a tool for controlling the RBC property [31–35]. Here this technique was employed to measure the elasticity change of RBC membrane upon increasing photooxidative damage. Fig. 3 shows the basic setup of the micropipette manipulation technique for the membrane elasticity measurement.

Briefly, tapered borosilicate glass micropipettes (A-M Systems, Inc., WA) with inner diameter ~ 2 μm were prepared by using the pipette puller (Model P-87, Sutter Instrument, CA) and the micro-forge (Model MF-900, Narishigue International USA, NY). The micropipette was filled with the PBS buffer and mounted in a 3D micromanipulator (Newport Corp., CA) with submicron control attached to the bright-field microscope. The micropipette tip was inserted inside the microchamber, which was made by two coverslip slits (Fig. 3(f)). The chamber was filled with PBS buffer with 0.1% BSA and RBC samples. The pressure of the micropipette was controlled with homemade water reservoirs' height change manually and monitored by an in-line pressure transducer (Validyne Engineering Corp., CA). Live images of the RBCs under the photooxidative process were recorded using the CCD camera with a home-built LabVIEW program which allows recording the live time and

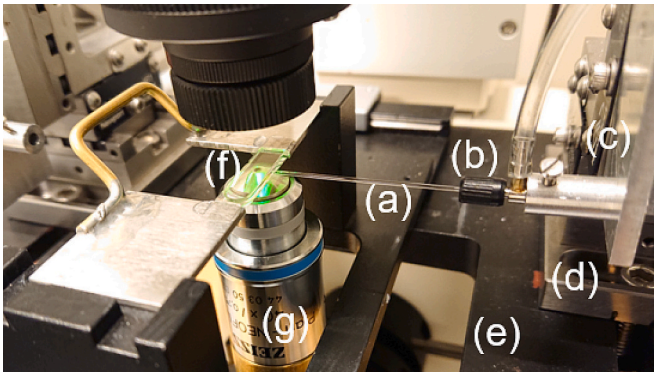

Fig. 3. Micropipette stage view: micropipette (a) is mounted via a chuck (b) in a custom-built holder (c), mounted on a stage micrometer (d) bolted firmly to the microscope platform (e). The image of the pipette tip in the microchamber (f), which is made by two pieces of coverslip slits, is viewed via a 40× objective lens (g).

pressure in the same frame.

The shear modulus μ was calculated by measuring the projection membrane length L inside the micropipette as a function of the aspiration pressure ΔP such that [35],

$$\Delta P = \left(\frac{\mu}{R_p}\right) \bullet \left[\left(\frac{2L}{R_p} - 1\right) + ln\left(\frac{2L}{R_p}\right)\right] \quad (2)$$

where R_p is the inner radius of the micropipette. As a control, the RBC shear modulus μ (= 6.72 ± 0.21 × 10^{-6} N/m) was determined by applying continuous aspiration pressure between ~20 and 40 Pa in isotonic PBS buffer (Supporting Information, Fig. S2). The average value showed an excellent agreement with the reference result, 6.6 ± 1.2 × 10^{-6} N/m [35]. Therefore, to obtain proper shear modulus under RBC photooxidation, four different aspiration pressures of about 25, 30, 35, and 40 Pa were applied by using the statistical aspiration pressure change with the water reservoirs' heights. The average shear modulus was then calculated from five different RBCs measurements per each set of the four obtained values (n = 20). To avoid the error of the shear modulus calculation, the projection length L was always kept bigger than the pipette radius R_p, $L/R_p > 1$ [35]. To assure the equilibrium at each chosen pressure, the RBC projection length L was measured following 30 s after each target pressure was reached.

3. Results

3.1. RBC Morphological Changes

3.1.1. Photooxidative Damage

RBC morphology changes due to CisDiMPyP photoactivation were

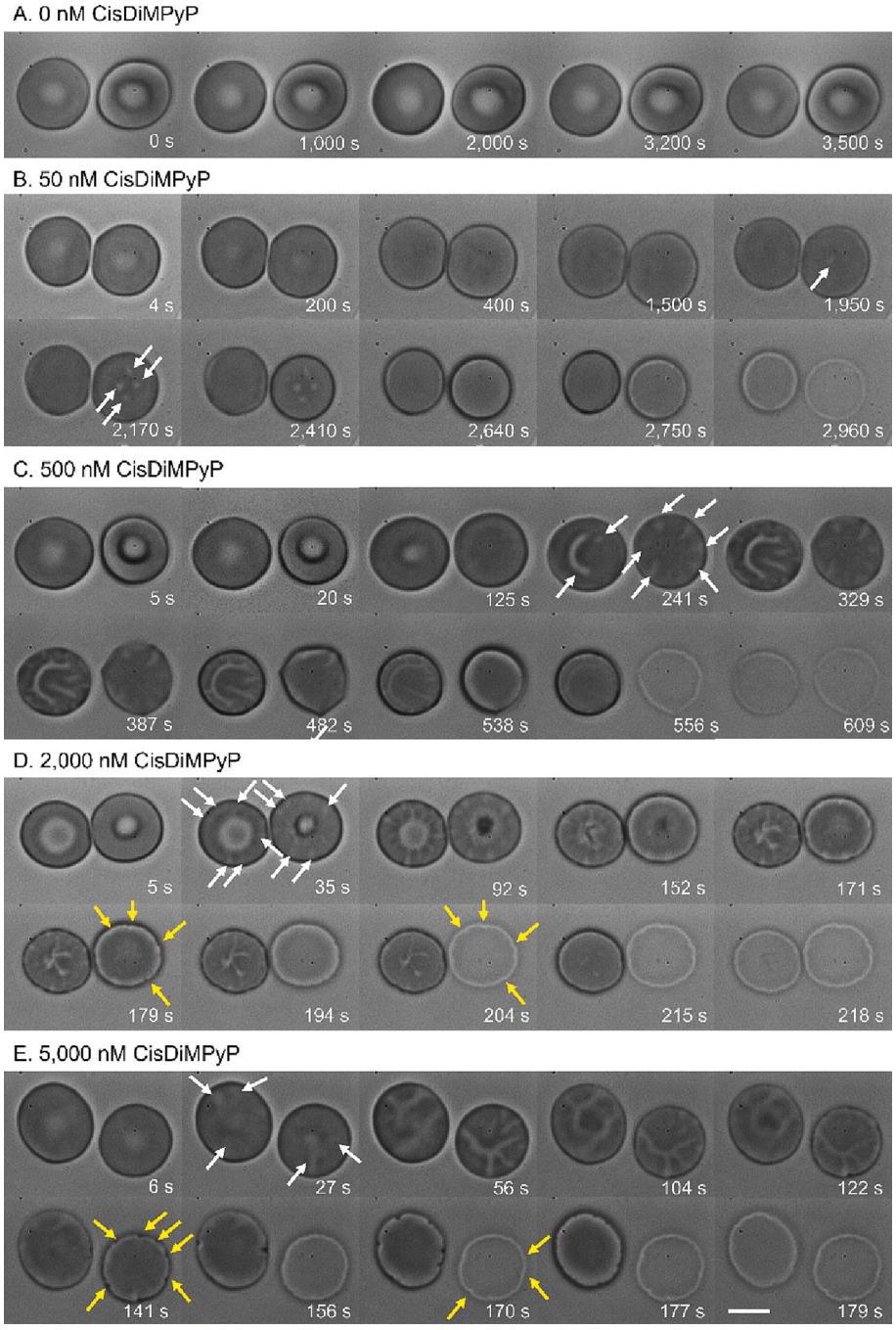

Fig. 4. RBC's morphological changes during photoactivation of CisDiMPyP at room temperature (20 ± 2 °C) over time (in seconds indicated in each frame) as seen by bright field microscopy. RBCs were mixed with (A) 0, (B) 50 nM, (C) 500, (D) 2000,and (E) 5000 nM CisDiMPyP and exposed to a constant light irradiance E_e of 26 J/m^2s over time. The white and yellow arrows show wrinkle-like patterns and high curvature spot(s) under photooxidative progress, respectively. To increase the visibility of these patterns, the contrast of the images was increased 40%. The scale bar is 5 μm. See the supplementary Video 1. (For interpretation of the references to colour in this figure legend, the reader is referred to the web version of this article.)

observed in real-time with constant light irradiance E_e of 26 J/m^{2}s at λ_{exc} = 546 ± 10 nm (Fig. 2A). Fig. 4 shows the times series of the morphological changes of RBCs dispersed in PBS buffer containing 0, 50, 500, 2000, and 5000 nM CisDiMPyP (see also supplementary Video 1 for 500 nM CisDiMPyP). Considering that the CisDiMPyP molecule has a preferential partition to the membrane surface (Fig. 1B) and applying the values of CisDiMPyP concentration and the constant E_e irradiance in eq. 1, the singlet oxygen $^1O_2$ production rate Q at λ_{exc} = 546 nm varied from 0.61 × 10^{-8} and 6.1 × 10^{-7} $^1O_2$ molecules/nm^{3}s (Fig. 2B), respectively.

The observation of a brighter area at the central part of RBC (Fig. 4A, 0–3500 s), associated with its regular biconcave shape, takes place at the initial short irradiation time: the first image of different CisDiMPyP porphyrin mixture (Fig. 4B – 4E, at 4–6 s). Of note, without irradiation, the presence of the porphyrin did not affect RBC morphology (data not shown).

In the case of lower concentrations of porphyrin (50 and 500 nM CisDiMPyP), with progression of irradiation, RBC shape and size becomes flat and bigger with a bright central area fading as observed in ~400 s in the presence of 50 nM porphyrin (Fig. 4B) and ~ 125 s in the presence of 500 nM porphyrin (Fig. 4C). Bright spots/patterns (white arrows) appeared after 1500 s and 125 s for 50 nM (Fig. 4B) and 500 nM CisDiMPyP (Fig. 4C), respectively. We observed a similar refraction pattern of wrinkles on the RBC membrane surface when it was squeezed in a narrow micropipette under an aspiration pressure (data not shown). Hence, we named it a wrinkle-like pattern. This pattern gradually increased to a larger area on the RBC membrane over time. The starting times of wrinkle-like patterns t_w for different CisDiMPyP concentrations were quantitatively analyzed using the plot of grayscale value histogram on Image J program (see Supporting Information, Fig. S3 and Section 3.1.4). These patterns disappeared around t_i ~ 2640 s for 50 nM CisDiMPyP (Fig. 4B) and t_i ~ 538 s for 500 nM CisDiMPyP (Fig. 4C, right-side RBC) followed by the decrease in the gray level of RBC when compared to the background. We consider that such contrast loss is due to hemolysis at a certain irradiation time (Fig. 4B: t_i ~ 2800–3000 s; Fig. 4C: t_i ~ 540–610 s), i.e., the formation of pores or tears in the membrane because of the continuous photooxidation, thus allowing the material exchange between intracellular components, mainly hemoglobin, and PBS buffer from the extracellular space.

In contrast, the photooxidative damage of higher porphyrin concentrations (2000 and 5000 nM CisDiMPyP) did not cause an increase in RBC membrane area in Fig. 4D and E (see Section 3.1.4 in detail). The morphological changes occurred faster than previously observed for lower porphyrin concentrations (Fig. 4B and C). More specifically, at t_i ~ 150–170 s for 2000 nM CisDiMPyP (Fig. 4D) and t_i ~ 30–60 s for 5000 nM CisDiMPyP (Fig. 4E), the discoid shape was lost. Meanwhile, the wrinkle-like patterns (white arrows) started much earlier at t_i < 35 s for 2000 nM and t_i < 27 s for 5000 nM CisDiMPyP (Fig. 4D, and E). And, eventually, hemolysis occurred at t_i ~ 180–220 s (Fig. 4D) and t_i ~ 140–180 s (Fig. 4E, see statistical data of hemolysis time in Section 3.1.3).

For these higher singlet oxygen production rates (2000 and 5000 nM CisDiMPyP), one can highlight: i) the appearance of wrinkle-like patterns at t_i ~ 30 s (Fig. 4D and E) happened simultaneously with the flattening process (in the case of lower singlet oxygen production rates, it was a continuous formation "after" the membrane area increase, see Fig. 4B and C); ii) high curvature spots appeared around the edge of RBC membrane (yellow arrows, Fig. 4D and E); and iii) hemolysis took place briefly after the development of the high curvature spots, Fig. 4D and E.

3.1.2. *The Effects of Singlet Oxygen Quencher Sodium Azide (NaN_3) on RBC Photooxidative Damage*

To understand the effect of CisDiMPyP photooxidative impact on RBC in more detail, we investigated the effects of sodium azide (NaN_3), a singlet oxygen quencher [36–41]. Fig. 5 shows RBC's morphological changes under the same light irradiance E_e of 26 J/m^{2}s at λ_{exc} = 546 ± 10 nm with 0, 500 and 5000 nM CisDiMPyP in the presence of 10 mM NaN_3.

The presence of 10 mM NaN_3 did not affect RBC morphology under the same irradiation condition (Fig. 5A). Incubation in the presence of 10 mM NaN_3 with CisDiMPyP showed similar RBC morphological changes (Fig. 5B and C) as observed in the absence of NaN_3 (Fig. 4).

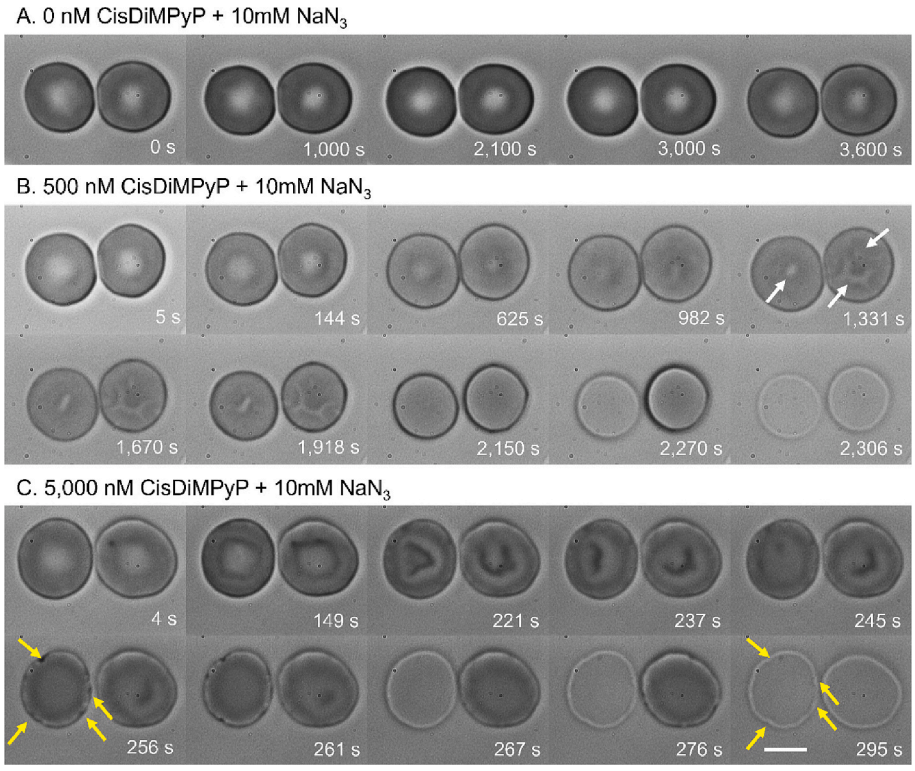

Fig. 5. RBC's morphological changes under the photoactivation of CisDiMPyP in the presence of 10 mM NaN_3 at room temperature (20 ± 2 °C) over time. RBCs were mixed (A) 0 nM, (B) 500 nM, and (C) 5000 nMCisDiMPyP, containing 10 mM NaN_3 during the constant irradiance of 26 J/m^{2}s over time. The white and yellow arrows show the appearance of wrinkle-like patterns and high curvature spot(s) during the photooxidative damage progression. To increase the visibility of these patterns, the contrast of the images was increased 40%. The scale bar is 5 μm. (For interpretation of the references to colour in this figure legend, the reader is referred to the web version of this article.)

However, it showed a significant time delay for all photodamage steps (Fig. 5B and C). In the absence of NaN_3, 500 nM CisDiMPyP induced photohemolysis at ~540–610 s (Fig. 4C), while the presence of 10 mM NaN_3 delayed it to ~2200–2300 s (Fig. 5B). About 100 s delay of photohemolysis was also observed in higher porphyrin concentration of 5000 nM CisDiMPyP, between absence (Fig. 4E, t_i ~ 160–180 s) and presence of 10 mM NaN_3 (Fig. 5C, t_i ~ 270–300 s, and see Section 3.1.3 in detail).

3.1.3. RBC Hemolysis Time under the CisDiMPyP Photoactivation

To validate the induction of RBC hemolysis due to CisDiMPyP photoactivation statistically, a higher number of RBCs ($n > 25$) were observed by using a lower magnification of the microscope with the same light irradiance E_e of 26 J/m^{2}s at $\lambda_{exc} = 546 \pm 10$ nm. Fig. 6A shows, as example, the dynamic hemolysis events of RBCs in 50 nM CisDiMPyP solution over time (see also supplementary Video 2 for 50 nM CisDiMPyP).

The average hemolysis times t^*_{lys} for different photooxidative damage levels of 50, 500, 2000, and 5000 nM CisDiMPyP in the absence of NaN_3 were plotted in Fig. 6B (open circles). t^*_{lys} value against singlet oxygen $^1O_2$ production rate, Q, on the log-log scale plot showed a trend of slope: increasing Q value induced continuous decrease of t^*_{lys} value. Further, the effect of 10 mM NaN_3 on the average hemolysis time t^*_{lys} of RBC was also measured for each CisDiMPyP concentration (Fig. 6B - solid circles) and we found that t^*_{lys} in the presence of 10 mM NaN_3 showed a similar slope trend, but a longer hemolysis time. Therefore, the presence of 10 mM NaN_3 data was replotted to overlap in the absence of NaN_3 plot data by multiplying a correction factor (CF) of 0.24 to Q (Fig. 6C). In this figure, Q_{CF} correction factor was distinguished as the estimated Q value for the NaN_3 quenching effects. From the estimation of the singlet oxygen production rate Q, this suggested that the efficiency of CisDiMPyP photooxidative damage of hemolysis was directly reduced to ~24% (4-folds) by adding 10 mM NaN_3.

3.1.4. RBC Membrane Area Change under the CisDiMPyP Photoactivation

RBC morphological changes induced by CisDiMPyP photoirradiation in the higher magnification images (Figs. 4 and 5), were analyzed for RBC discoid area A_d (2-dimensional profile area) over irradiation time t_i, $A_d(t_i)$.

Fig. 7A shows the normalized RBC discoid area $A_d(t_i)/A_0$ with respect to the initial area A_0 as a function of the normalized irradiation time t_i/t_{lys}, with the individual irradiation time t_{lys} ($\neq t^*_{lys}$) for hemolysis.

Interestingly, the RBC discoid area $A_d(t_i)$ calculated at 50 nM and 500 nM CisDiMPyP (Fig. 7A), open blue and black symbols, respectively, was similar but with a delay in the photodamage steps. Specifically, change of A_{max} was ~1.1 fold from the initial size A_0 irrespective of different photooxidative damages caused by different irradiation times and concentrations, followed by the immediate appearance of wrinkle-like patterns. The normalized average irradiation time associated with the beginning of wrinkle-like patterns t_w/t_{lys} is shown by dashed lines, i.e. $t_w/t_{lys} = 0.51 \pm 0.08$ for 50 nM (blue dashed line) and 0.27 ± 0.08 for 500 nM CisDiMPyP (black dashed line), n > 18 RBCs. These values were obtained quantitatively from the image analysis of grayscale value histogram (see Supporting Information, Fig. S3). Next, $A_d(t_i)$ decreased to its initial value ($A_d(t_i)/A_0 = 1$) up to ~70% of photooxidation progress (red arrow in Fig. 7A). Finally, a further reduction in area was achieved $A_d(t_i)/A_0 = 0.75 \pm 0.01$ (blue star symbol, Fig. 7A) immediately prior to hemolysis.

In contrast, no area increase $A_d(t_i)$ was observed with either 2000 nM (Fig. S4, open pink symbols) or 5000 nM CisDiMPyP induced photooxidative damage (Fig. 7A, open red symbols), while, the wrinkle-like patterns were observed much earlier, specifically $t_w/t_{lys} = 0.17 \pm 0.02$ (2000 nM: Fig. S4, red dashed line) and 0.14 ± 0.03 (5000 nM: Fig. 7A,

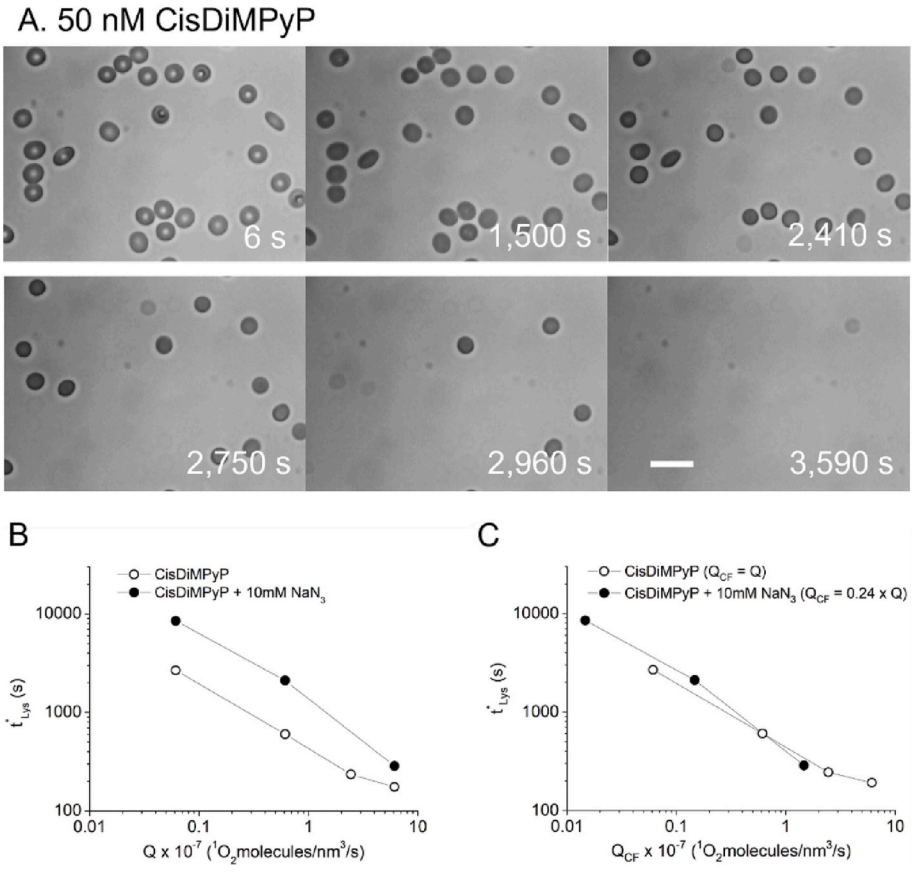

Fig. 6. RBC hemolysis events (n > 25) under the CisDiMPyP photoirradiation. (A) RBC hemolysis events under the photoactivation of 50 nM CisDiMPyP over time. To increase the visibility of hemolysis, the contrast of the images was increased 40%.The scale bar is 20 μm. See the supplementary Video 2. (B) The average hemolysis time t^*_{lys} vs. Q plot (absence of NaN_3: open circles; and presence of NaN_3: closed circles). Each plot was obtained from the average hemolysis time t^*_{lys} of three sets of measurements (except 50 nM CisDiMPyP in presence of NaN_3: one set of 31 RBCs measurements). The standard deviation was the same or smaller than the symbol size.(C) To overlap both results of hemolysis time in absence and presence of NaN_3 in the trend curve, NaN_3 mixture data were adjusted by applying the correction factor (CF) of 0.24 to the CisDiMPyP concentration.

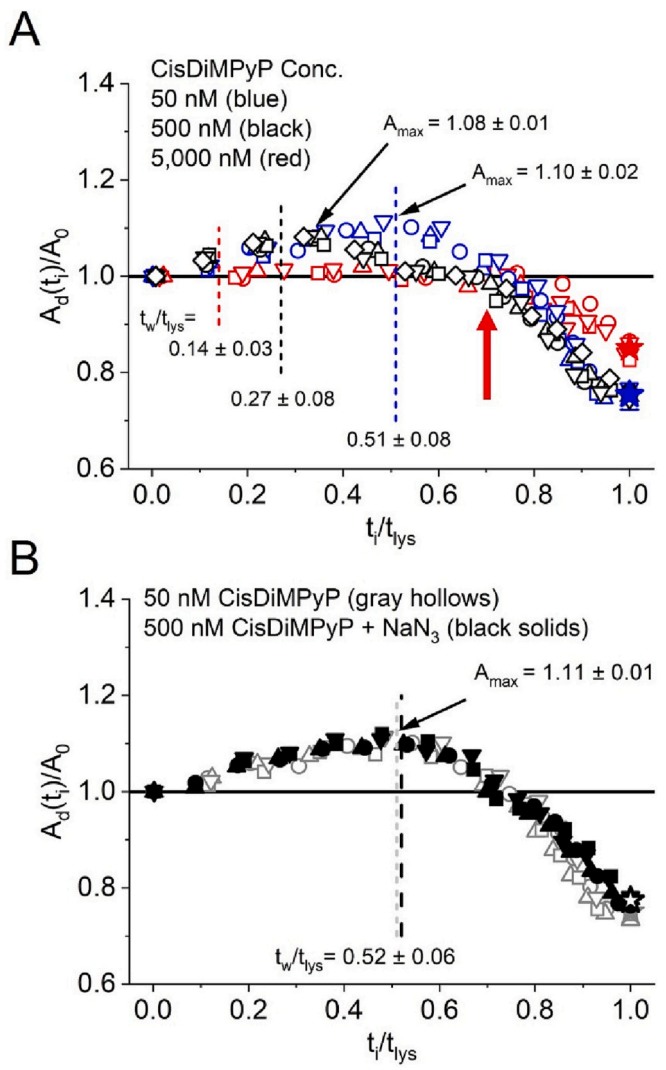

Fig. 7. (A) Normalized RBC's area as a function of the photoactivation of CisDiMPyP at 20 °C. Blue, black,and red open symbols show 50, 500, and 5000 nM CisDiMPyP area change data during the constant irradiance of 26 J/m^{2}s over time. The normalized average maximum area expansion A_{max} (A_{max}/A_0: 1.10 ± 0.02 for 50 nM CisDiMPyP; and A_{max}/A_0: 1.08 ± 0.01 for 500 nM CisDiMPyP) and the normalized average final area before hemolysis A_{lys} (blue star symbol of $A_{lys}/A_0 = 0.75 \pm 0.01$ for 50 nM CisDiMPyP; and red star symbol of $A_{lys}/A_0 = 0.85 \pm 0.02$ for 5000 nM CisDiMPyP) are shown in the figure. The blue, black, and red short-dashed lines show the average ($n > 18$ RBCs) of the start of wrinkle-like pattern observation, t_w/t_{lys}, for 50, 500, and 5000 nM CisDiMPyP, respectively. The horizontal solid black line shows $A_d/A_0 = 1$. Four individual measurement results from RBCs were plotted with different symbols for each concentration of CisDiMPyP ($n = 4$). (B) Normalized RBC area changes under the photoactivation of CisDiMPyP in the presence of NaN_3. Black solid symbols show 500 nM CisDiMPyP in the presence of NaN_3 during the constant irradiance of 26 J/m^{2}s over time. For comparison, gray open symbols, 50 nM CisDiMPyP in the absence of NaN_3, were also replotted from (A). The normalized average maximum area expansion A_{max}/A_0 (= 1.11 ± 0.01), the start of wrinkle-like patterns t_w/t_{lys} (back dashed line), and the final area A_{lys}/A_0 (= 0.77 ± 0.01, black open star symbol) before hemolysis also showed. (For interpretation of the references to colour in this figure legend, the reader is referred to the web version of this article.)

red dashed line). Photohemolysis happened when $A_d(t_i)/A_0$ was circa 0.85–0.87 (red star symbols, Fig. S4 and 7A).

Changes in RBC discoid area $A_d(t_i)$ in the presence of 10 mM NaN_3 with 500 nM CisDiMPyP were analyzed over irradiation time t_i (Fig. 7B). Interestingly the resulting data overlapped with a similar increase in area and reduction trend of 50 nM CisDiMPyP in the absence of 10 mM NaN_3 (Fig. 7B). The similarity between the photodamage, averaged hemolysis time t^*_{lys} and corrected singlet oxygen production rate Q_{CF} caused by two different conditions (i) 500 nM CisDiMPyP in the presence of 10 mM NaN_3 and (ii) 50 nM CisDiMPyP in the absence of 10 mM NaN_3, was also observed in the $A_d(t_i)$ in Fig. 7B and 6C. The averaged initiation of wrinkle-like patterns ($t_w/t_{lys} = 0.52 \pm 0.06$, black long dashed line in Fig. 7B) also showed a similar value in samples treated with 50 nM CisDiMPyP in the absence of 10 mM NaN_3 ($t_w/t_{lys} = 0.51 \pm 0.08$, gray dashed line in Fig. 7B).

3.2. RBC Membrane Elasticity Depending on the Photooxidative Damage Level

3.2.1. The Shear modulus of the RBC Membrane

The elasticity/rigidity of the RBC membrane can be quantified by shear modulus, which was measured by using the micropipette aspiration technique. Fig. 8A shows the measured shear modulus of RBC exposed to 50 nM CisDiPyP for each irradiation time t_i between 0 and 800 s. The same irradiance ($E_e = 26$ J/m^{2}s, $\lambda_{exc} = 546$ nm) was applied, corresponding to $Q = 0.61 \times 10^{-8}$ $^1O_2$ molecules/nm^{3}s (i.e., the total flux between 200 s and 700 s varied from 1.22×10^{-6} to 4.27×10^{-6} $^1O_2$ molecules/nm^3) to correlate with the experimental results presented in Section 3.1. Accordingly, photoactivated RBCs in the presence of 50 nM CisDiMPyP displayed an increase in area until the initiation of wrinkle-like patterns at $t_w/t_{lys} = 0.51 \pm 0.08$ (blue dashed line:$t_i \sim 1360 \pm 220$ s, $n = 18$ in Fig. 7A), which is much longer irradiation time than the range of this measurement ($t_i \leq 800$ s).

The shear modulus μ ($= 6.30 \pm 0.2 \times 10^{-6}$ N/m) for 0 s irradiation in Fig. 8A is in agreement with the photosensitizer-free RBC shear modulus, $6.72 \pm 0.21 \times 10^{-6}$ N/m (see the Supporting Information, Fig. S2), and reference data, $6.67 \pm 1.21 \times 10^{-6}$ N/m [35]. This suggests that the mixing (adsorption) and the washing (desorption) process of CisDiMPyP without irradiation did not affect the shear modulus. Till ~200 s irradiation time t_i ($t_i/t_{lys} \sim 0.08 \pm 0.01$), oxidative damage did not cause any significant increase of the shear modulus μ. However, μ was significantly increased by increasing t_i. At $t_i = 700$ s ($t_i/t_{lys} \sim 0.27 \pm 0.03$) the μ reached a value of $(8.2 \pm 0.3) \times 10^{-6}$ N/m. Afterward, we could not measure the shear modulus at $t_i = 800$ s ($t_i/t_{lys} \sim 0.31 \pm 0.03$) because of ruptured RBCs during the washing steps of centrifugation (striped area in Fig. 8A). We consider that the 500 *g* force during the centrifugation is enough to disrupt the already photooxidatively damaged RBC membrane.

To evaluate the dynamic photooxidative damage on the membrane stiffness of RBCs mixed with 500 nM CisDiMPyP without washing steps were investigated. The initial aspiration pressure of 29 Pa caused the RBC membrane to deform (Fig. 8B-i, inside of yellow circle) possibly because of its resilience, which recovered quickly after releasing the aspiration pressure to 0 Pa, e.g. the time required for the RBC membrane projection to decrease in length by 50% is about 0.3 s [42]. However, it did not recover after continuous irradiation (~300 s of $E_e = 26$ J/m^{2}s and $\lambda_{exc} = 546$ nm) suggesting that the viscoelasticity of the membrane suddenly increased, i.e. plastic-like rigidity (Fig. 8B-ii and iii, inside of yellow circles).

4. Discussion

In this study we measured dynamic deformations and changes in mechanical property of RBCs and we found that there were distinguishable characteristic effects, depending on the photooxidative damage levels caused due to CisDiMPyP irradiation over time. To quantify the level of photooxidative damage of RBC, we estimated singlet oxygen $^1O_2$ production rate Q as the primary oxidative species. Notably, the diffusion coefficient (D) and the lifetime (τ) of $^1O_2$ in the lipid bilayer are, respectively, on the order of 0.7–1.4 $\times$ 10^{-5} cm^2/s and 0.4 μs

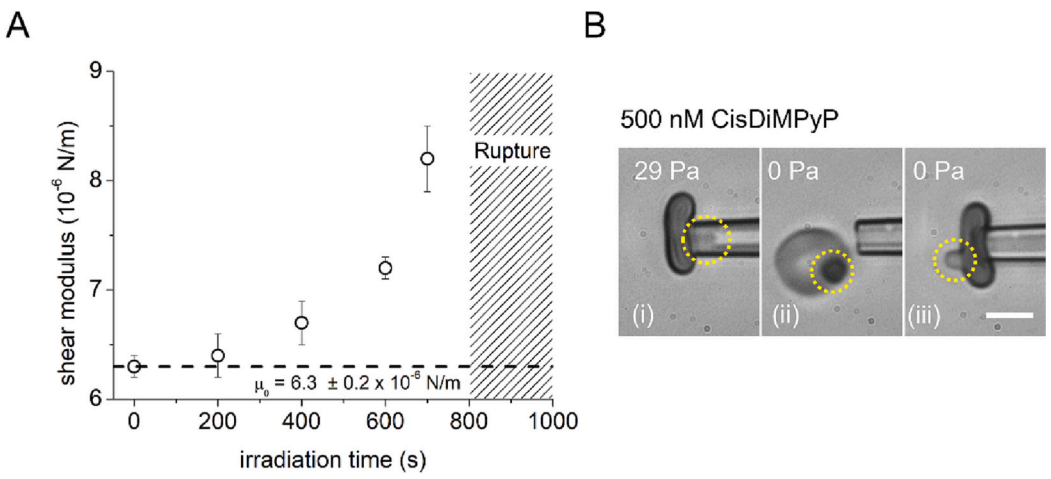

Fig. 8. RBC shear modulus increases as the degree of photooxidative damage increases. (A) The average of RBCs (n = 5) shear modulus under photoactivation of 50 nM CisDiMPyP, as a function of irradiation time t_i at 20 °C (the total singlet oxygen flux varied from 1.22 × 10^{-6} to 4.27 × 10^{-6} $^1O_2$ molecules/nm^3 between 200 s and 700 s). The striped area shows the limitation of the shear modulus measurement due to the RBC's membrane rupture during the sample preparation process. The black dashed line shows the shear modulus value, 6.3 ± 0.2 × 10^{-6} N/m, of the non-irradiated RBC sample, i.e. irradiation time 0 s. The constant irradiance E_e of 26 J/m^{2}s was applied for all measurements.(B) Plastic-like rigidity of RBC membrane induced by photooxidative damage of 500 nM CisDiMPyP at 20 ± 2 °C. Each picture shows, (i) 29 Pa aspiration to form projection in the yellow dashed circle, (ii) aspiration pressure release, i.e. 0 Pa, after ~300 s photodamage (E_e = 26 J/m^{2}s, λ_{exc} = 546 nm), and (iii) stable deformation from the plastic-like rigidity, i.e. non-resilient of RBC membrane. The scale bar is 5 μm.

[38,39], resulting in a radial diffusion length ($L = \sqrt{D\tau}$) of ~20 nm. Therefore, as porphyrin is homogeneously distributed in the membrane, the $^1O_2$ generated can diffuse and interact with both lipids and proteins in the outer and inner leaflet of the bilayer, since a leaflet is about 2–3 nm thick [45,46].

Here we propose three levels of photooxidative damage: mild, moderate, and severe (Fig. 9).

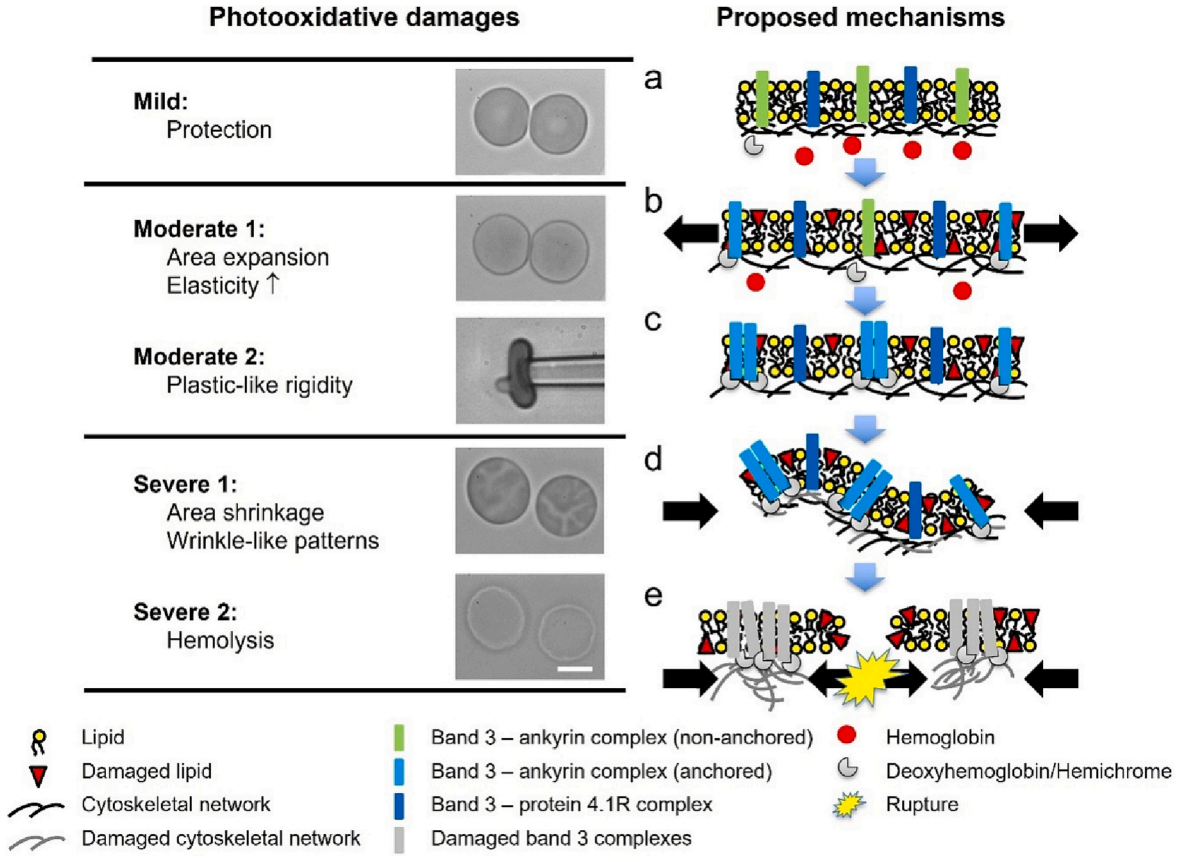

Fig. 9. Summary of RBC damage depending on the CisDiMPyP photooxidative damage levels and the proposed mechanism for each damage. The progress of RBC photooxidative damage is classified as mild, moderate, and severe damage. The black arrows in the proposed mechanism image show the compressive/expansion tension on the membrane. The yellow star indicates the break of the cytoskeletal network under the localized compressive tensions. The scale bar in the picture shows 4.6 μm for the plastic-like rigidity picture and 5 μm for the rest of the pictures. (For interpretation of the references to colour in this figure legend, the reader is referred to the web version of this article.)

4.1. Mild Photooxidative Damage – Prevention from Photooxidative Damage

Under mild photooxidative damage using the lowest studied concentration of 50 nM CisDiMPyP or 500 nM CisDiMPyP with 10 mM NaN_3,we observed steady/prevention properties of RBC membrane: constant size of RBC membrane, $A_d(t_i)/A_0 \approx 1$ ($t_i/t_{lys} < \sim 0.08$ in Fig. 7A and B) and constant shear modulus, $\mu \approx 6.30 \times 10^{-6}$ N/m (t_i = 0–200 s in Fig. 8A). Repetitive irradiations also showed the prevention of photooxidative damage in a low $^1O_2$ density regime (Supporting Information, Fig. S5). One of the possibilities for the prevention of damage is antioxidant enzymes and/or non-enzymatic compounds present in RBC. It is well-known that reduced glutathione (GSH) is oxidized to glutathione disulfide (GSSG) to protect the cell membrane from ROS attack and prevent lipid peroxidation [2,13,43]. Glutathione peroxidases, such as GPx1 and GPx4, use GSH as a substrate to reduce lipid hydroperoxides and prevent further damage to the membrane (Fig. 9, **proposed mechanism a**) [44].

4.2. Moderate Photooxidative Damages –RBC Membrane Area Expansion, Shear Modulus Increase, and Plastic-Like Rigidity

With increasing photooxidation (i.e.irradiation time t_i), RBC loses its biconcave disc shape: morphological change from the biconcave shape ($t_i > \sim 200$ s of 50 nM CisDiMPyP in Fig. 4B, and $t_i > \sim 20$ s of 500 nM CisDiMPyP in Fig. 4C). At the same time, the discoid area size $A_d(t_i)$ is increased up to $A_{max}/A_0 = 1.10 \pm 0.02$ at $t_i/t_{lys} \approx 0.51$ (50 nM CisDiMPyP) and $A_{max}/A_0 = 1.08 \pm 0.01$ at $t_i/t_{lys} \approx 0.33$ (500 nM CisDiMPyP) in Fig. 7A. We propose that this morphological change could be related to lipid oxidation as discussed below (Fig. 9, **proposed mechanism b**).

The effect of photooxidative damage on the lipid bilayer model systems composed of phospholipids has been widely investigated. For example, the presence of oxidized lipids in the bilayer (in situ generation or already sensitized) could increase the lipid area due to hydroperoxide formation and even cause the complete rupture of the membrane due to oxidized truncated lipids by-product formation [6,7,47,48]. Therefore, the lipid peroxidation at the RBC membrane may play a key role in the expansion of area and morphological changes from biconcave to flat discoid shape. In fact, cholesterol (25% of total RBC lipids) and unsaturated lipids (around 73% of all RBC lipids), which are well-known targets for singlet oxygen $^1O_2$ could be damaged by the photooxidative mechanism [47–52]. Thus, several lipids can be oxidized in the RBC membrane.

However, the damage of membranes containing only lipids (mimetic systems) is not enough to explain the change in mechanical property observed here, i.e., the increase in shear modulus (Fig. 8A) and the decrease in the RBC membrane fluctuation (see Supporting Information, Fig. S6), since the oxidative damage of membrane containing only lipids lead to an increase in membrane fluctuation. Thus, one should consider the impact of the photodamage on the cytoskeletal proteins in RBC to interpret the increase of RBC's shear modulus and decrease of membrane fluctuation. It is known that the spectrin tetramer bundles generate a quasi-hexagonal symmetry with triangulated scaffoldings at the cytoskeletal network [53,54]. They are anchored with band 3-based complexes, i.e., band3 - ankyrin complex and band3 - protein 4.1R junctional complex [54–57]. It is also known that the spectrin bundles can stretch (unfolded) and detach at the anchoring spots of band 3 – based complexes [58–60]. Therefore, we consider that this mechanical flexibility of the cytoskeletal network formation achieves a quick recovery to the original shape after removing the shear/isotropic tension to RBC membrane [42]. Thus, one can suggest that under moderate photooxidative damage, there is uniform stretching of spectrin bundles (isotropic expansion) causing expansion of RBC membrane and hence its deformation (Fig. 9, **proposed mechanism b**).

Therefore, even though the photodamaged lipid causes the decrease in membrane rigidity, the isotropic expansion of cytoskeletal networks would counterbalance/dominate with the net result being the increase of membrane stiffness.

We also observed that photodamage caused an inflexibility of the membrane's mechanical function, i.e., plastic-like rigidity (Fig. 8B). Although the plastic-like rigidity formation of RBC membrane was observed in previous studies, the mechanism is still unknown [3,4]. To explain the non-flexibility of RBC membrane, we speculate that the flexibility of the cytoskeletal network function could have been diminished by the permanent attachment of the cytoskeletal network at the anchoring spots of band 3 – based complexes, including the photodamaged hemoglobin. Until now it is known that 1) band 3 with ankyrin complex has reversible binding sites at the N-terminal for deoxyhemoglobin and denatured hemoglobin (hemichrome) [54], 2) band 3-hemoglobin interaction has important roles in oxidative damage and oxygenation [61–63], and 3) about one-third of band 3 molecules are diffusing in the lipid membrane freely [64,65]. Therefore one can suggest that the inflexibility of the cytoskeletal network was derived from the interaction between band 3 and hemoglobin (Fig. 9, **proposed mechanism c)**. However, to demonstrate this mechanism, further experimental data is required.

4.3. Severe Photooxidative Damages – RBC Membrane Wrinkle-Like Patterns and High Curvature Spots Formation Toward Hemolysis

When the area reached the peak A_{max}/A_0 ($t_i/t_{lys} \approx 0.5$ for 50 nM CisDiMPyP and $t_i/t_{lys} \approx 0.3$ for 500 nM CisDiMPyP (Fig. 7A)), wrinkle-like patterns were initiated on the surface of RBC membrane. Therefore, there is a correlation between this pattern formation and $A_d(t)$ decrease caused by CisDiMPyP concentrations. A possible interpretation of the formation of wrinkle-like patterns could be an impact caused by spectrins cross-linking due to photooxidative damage. It is known that the cross-linking of spectrins under photooxidative stress happens much earlier than the cross-linking of band 3 proteins [23]. Therefore, before the final step of the cross-linking of band 3 proteins, the cross-linking of spectrins could start pulling back (retraction: Fig. 9, **proposed mechanism d**) the stretched spectrin bundles against the isotropic expanding tension of photodamaged lipid membrane (Fig. 9, **proposed mechanism b)**. Hence, there is an imbalance between the region of cytoskeletal network (shrinkage) and lipid membrane (expansion).This could also explain why RBC membrane composed of highly incompressible materials does not require large isotropic tensions to create a wrinkle-like pattern [34]. It has been reported that 50 mM NaN_3 could reduce the bilirubin-photosensitized spectrin's cross-linking of RBC approximately 3-folds [66]. Therefore, the delay of wrinkle-like patterns beginning from 165 ± 38 s ($t_w/t_{lys} = 0.27 \pm 0.08$, $n = 20$) to 1040 ± 64 s ($t_w/t_{lys} = 0.52 \pm 0.06$, n = 20) by mixing 10 mM NaN_3 in 500 nM CisDiMPyP in Fig. 7B could be correlated with the delay of spectrin cross-linking under photooxidative damage due to CisDiMPyP irradiation. Meanwhile, wrinkle-like patterns appeared without increasing the RBC membrane area at high concentrations of porphyrin under irradiation, such as 2000 and 5000 nM CisDiMPyP (Fig. S6 - pink open symbols and Fig. 7A - red open symbols). This could be interpreted as the simultaneous formation of spectrins cross-linking when the photooxidative damaging of membrane lipids (area expansion) and irreversible anchoring of the spectrin bundles' attachment (inflexibility) occurred.

During severe photooxidative damage, we suggest that the spectrin complex breaks due to crossing the limit of spectrin network formation. Using differential scanning calorimetry (DSC) measurements, we found that severe photooxidative damage caused complete denaturation of cytoskeletal network proteins: spectrin complex (A-transition), 2.1, 4.1 and 4.2 bands with different types of glycophorin (B_1-transition), band 3 N-terminal segment of the cytoplasmic domain (B_2-transition), and anion-transporting domain of band 3 (C-transition) (See Supporting Information, Fig. S7). In the case of high levels of photooxidative damage, we also observed high curvature deformations, yellow arrows

in Fig. 4D and E (2000 and 5000 nM CisDiMPyP) and in Fig. 5C (5000 nM CisDiMPyP with 10 mM EDTA). Thus, under a highly damaged cytoskeletal network of the cross-linking of band 3 complexes and the breaking of spectrin complex, it could be the evidence of a localized high tension in the membrane leading to RBC hemolysis. (Fig. 9**, proposed mechanism e)**.

Finally, the correlation between the most frequent hemolysis time t^*_{lys} and the singlet oxygen $^1O_2$ production rate Q from CisDiMPyP photosensitizer was demonstrated in Fig. 6B and C. Interestingly it showed a linear-like slope on the log-log scale plot. Further, in the presence of 10 mM NaN3, a well-known singlet oxygen quencher, we found the increase in hemolysis time of about 4-folds. This explains that the photooxidative damage from singlet oxygen plays a key role in hemolysis here. Although azide ion can effectively and physically quench singlet oxygen [36,37], it can also react with hydroxyl radical $HO^{\bullet}$, forming a reactive species of azide radical $N_3^{\bullet}$ [67–69]. Even though CisDiMPyP has a high quantum yield of $^1O_2$ generation (= 0.74 in methanol and 0.2 in PBS) from type II energy transfer reaction as mentioned above, this porphyrin could also produce many different types of reactive oxygen species (ROS) from type I electron transfer reaction, e.g. superoxide anion $O_2^{\bullet-}$ and hydroperoxide anion HO_2^-, recognized as poorly reactive oxidants [70]. Thus, for future investigations of other ROS products and their effects on RBC membrane, applying free radical scavengers (e.g. vitamin E, *N*-acetylcysteine- NAC, GSH) or metal chelators (e.g. desferal, diethylene triamine pentaacetic acid - DTPA) would be helpful [71–74].

5. Concluding Remarks

Concerning the lack of relationship between the initial steps of membrane damage induced by photooxidation and the sequence of events that lead to RBC hemolysis, we were able to demonstrate that different alterations in RBC morphology occurs depending on the level of oxidative damage. We propose three levels of photooxidative damage 1) mild oxidative damage that occurred due to photoactivation of 50 nM and 500 nM CisDiMPyP at short irradiation times, 2) moderate oxidative damage by irradiating for longer times in the presence of 50 nM and 500 nM CisDiMPyP and 3) severe oxidative damage at low porphyrin concentrations irradiated for even longer times and for high porphyrin concentration. In the mild oxidative damage condition, no membrane flattening was detected. During moderate oxidative damage level, membrane flattening and expansion was observed, followed by increase in shear and bending modulus, and plastic-like rigidity. For severe oxidative damage, there were formation of wrinkle-like patterns and/or high curvature, membrane shrinkage followed by hemolysis.

Our findings of photooxidative damage in the RBCs promoted by CisDiMPyP can pave the way to better understand “natural” oxidation damages in vivo, like aging, and also be useful to elucidate the mechanism of different diseases. Besides those natural implications, it is also important to note that these findings can help develop photodynamic therapy (PDT) in which the use of photosensitizers is essential and to understand possible drawbacks of this technique.

CRediT authorship contribution statement

Gustavo Scanavachi: Conceptualization, Methodology, Investigation, Formal analysis, Validation, Visualization, Writing – original draft, Writing – review & editing. **Koji Kinoshita:** Conceptualization, Methodology, Investigation, Formal analysis, Validation, Visualization, Writing - original draft, Writing - review & editing. **Tayana M. Tsubone:** Investigation, Writing – original draft, Writing – review & editing. **Rosangela Itri:** Conceptualization, Supervision, Writing – original draft, Writing – review & editing.

Declaration of Competing Interest

The authors declare that they have no known competing financial interests or personal relationships that could have appeared to influence the work reported in this paper.

Data availability

Data will be made available on request.

Acknowledgements

The authors thanks to prof Luis Bagatolli for his brilliant ideas and support during the initial experiments. GS acknowledges PhD scholarship from the Coordination for the Improvement of Higher Education Personnel (CAPES). RI is recipient from CNPq research fellowship. KK also acknowledges support from The São Paulo Research Foundation –FAPESP, Brazil, (project # 2021/13023-5) for a working visit to the University of Sao Paulo. KK, GS, and TT also acknowledge support from Ministry of Higher Education and Science, Denmark (6144-00066) for a working visit between the University of São Paulo and the University of Southern Denmark. The authors also thank prof Carlos Alvarez for the careful reading of the manuscript. The authors also thank Dr. Anwesha Sanyal for proofreading the manuscript.

Appendix A. Supplementary data

Supplementary data to this article can be found online at https://doi.org/10.1016/j.jphotobiol.2023.112754.

References

[1] R. Sender, S. Fuchs, R. Milo, Revised estimates for the number of human and bacteria cells in the body, PLoS Biol. 14 (2016) 1–14.
[2] V. Kuhn, L. Diederich, T.C.S.T. Keller, C.M. Kramer, W. Lückstädt, C. Panknin, T. Suvorava, B.E. Isakson, M. Kelm, M.M. Cortese-Krott, Red blood cell function and dysfunction: redox regulation, nitric oxide metabolism, Anemia, Antioxid. Redox Signal. 26 (2017) 718–742.
[3] A. Sinha, T.T.T. Chu, M. Dao, R. Chandramohanadas, Single-cell evaluation of red blood cell bio-mechanical and nano-structural alterations upon chemically induced oxidative stress, Sci. Rep. 5 (2015) 9768.
[4] R.P. Hebbel, A. Leung, N. Mohandas, Oxidation-induced changes in microrheologic properties of the red blood cell membrane, Blood 76 (1990) 1015–1020.
[5] T.M. Tsubone, W.K. Martins, C. Pavani, H.C. Junqueira, R. Itri, M.S. Baptista, Enhanced efficiency of cell death by lysosome-specific photodamage, Sci. Rep. 7 (2017) 6734.
[6] M. Sonoda, C.M. Krishna, P. Riesz, The role of singlet oxygen in the photohemolysis of red blood cells sensitized by phthalocyanine sulfonates, Photochem. Photobiol. 46 (1987) 625–631.
[7] R. Itri, H.C. Junqueira, O. Mertins, M.S. Baptista, Membrane changes under oxidative stress: the impact of oxidized lipids, Biophys. Rev. 6 (2014) 47–61.
[8] T.M. Tsubone, M.S. Baptista, R. Itri, Understanding membrane remodelling initiated by photosensitized lipid oxidation, Biophys. Chem. 254 (2019).
[9] M.J. Davies, Protein oxidation and peroxidation, Biochem. J. 473 (2016) 805–825.
[10] M. Gracanin, C.L. Hawkins, D.I. Pattison, M.J. Davies, Singlet-oxygen-mediated amino acid and protein oxidation: formation of tryptophan peroxides and decomposition products, Free Radic. Biol. Med. 47 (2009) 92–102.
[11] T.M. Tsubone, H.C. Junqueira, M.S. Baptista, R. Itri, Contrasting roles of oxidized lipids in modulating membrane microdomains, Biochim. Biophys. Acta Biomembr. 1861 (2019) 660–669.
[12] N. Watabe, Y. Ishida, A. Ochiai, Y. Tokuoka, N. Kawashima, Oxidation decomposition of unsaturated fatty acids by singlet oxygen in phospholipid bilayer membranes, J Oleo Sci 56 (2007) 73–80.
[13] W. Korytowski, A.W. Girotti, Singlet oxygen adducts of cholesterol: photogeneration and reductive turnover in membrane systems, Photochem. Photobiol. 70 (1999) 484–489.
[14] A.W. Girotti, Lipid hydroperoxide generation, turnover, and effector action in biological systems, J. Lipid Res. 39 (1998) 1529–1542.
[15] G.J. Bachowski, E. Ben-Hur, A.W. Girotti, Phthalocyanine-sensitized lipid peroxidation in cell membranes: use of cholesterol and azide as probes of primary photochemistry, J. Photochem. Photobiol. B 9 (1991) 307–321.
[16] A.W. Girotti, G.J. Bachowski, J.E. Jordan, Lipid peroxidation in erythrocyte membranes: cholesterol product analysis in photosensitized and xanthine oxidase-catalyzed reactions, Lipids 22 (1987) 401–408.
[17] H. Verweij, T.M. Dubbelman, J. Van Steveninck, Photodynamic protein cross-linking, Biochim. Biophys. Acta 647 (1981) 87–94.

[18] A.W. Girotti, Photosensitized cross-linking of erythrocyte membrane proteins. Evidence against participation of amino groups in the reaction, Biochim. Biophys. Acta 602 (1980) 45–56.
[19] B. Vilsen, H. Nielsen, Reaction of phenylhydrazine with erythrocytes. Cross-linking of spectrin by disulfide exchange with oxidized hemoglobin, Biochem. Pharmacol. 33 (1984) 2739–2748.
[20] A.A. Lamola, F.H. Doleiden, Cross-linking of membrane proteins and protoporphyrin-sensitized photohemolysis, Photochem. Photobiol. 31 (1980) 597–601.
[21] S. Beaton, R.A. McPherson, L. Tilley, Alterations in erythrocyte band 3 organization induced by the photosensitizer, hematoporphyrin derivative, Photochem. Photobiol. 62 (1995) 353–355.
[22] A.W. Girotti, Protoporphyrin-sensitized photodamage in isolated membranes of human erythrocytes, Biochemistry 18 (1979) 4403–4411.
[23] T.M.A.R. Dubbelman, A.F.P.M. Degoeij, J. Vansteveninck, Protoporphyrin-induced photodynamic effects on transport processes across the membrane of human-erythrocytes, Biochim. Biophys. Acta 595 (1980) 133–139.
[24] T.M.A.R. Dubbelman, A.W. Debruijne, J. Vansteveninck, Photodynamic effects of Protoporphyrin on red blood-cell deformability, Biochem Bioph Res Co 77 (1977) 811–817.
[25] M.G. Tozzi-Ciancarelli, A. Di Giulio, E. Troiani-Sevi, A. D'Alfonso, G. Amicosante, A. Oratore, Human erythrocyte damage at the initial stages of oxidative stress, Cell Biophys. 15 (1989) 225–234.
[26] E.F. Silva, C. Serpa, J.M. Dabrowski, C.J. Monteiro, S.J. Formosinho, G. Stochel, K. Urbanska, S. Simoes, M.M. Pereira, L.G. Arnaut, Mechanisms of singlet-oxygen and superoxide-ion generation by porphyrins and bacteriochlorins and their implications in photodynamic therapy, Chemistry 16 (2010) 9273–9286.
[27] M. Pineiro, A.L. Carvalho, M.M. Pereira, A. Gonsalves, L.G. Arnaut, S. J. Formosinho, Photoacoustic measurements of porphyrin triplet-state quantum yields and singlet-oxygen efficiencies, Chem. Eur. J. 4 (1998) 2299–2307.
[28] T.M. Tsubone, Z. Zhang, R. Goyal, C. Santacruz, W.K. Martins, J. Kohn, M. S. Baptista, Porphyrin-loaded TyroSpheres for the intracellular delivery of drugs and Photoinduced oxidant species, Mol. Pharm. 17 (2020) 2911–2924.
[29] W. Caetano, P.S. Haddad, R. Itri, D. Severino, V.C. Vieira, M.S. Baptista, A. P. Schröder, C.M. Marques, Photo-induced destruction of giant vesicles in methylene blue solutions, Langmuir 23 (2007) 1307–1314.
[30] J.R. Lakowicz, Principles of Fluorescence Spectroscopy, Third ed., Springer, New York, 2006.
[31] K. Kinoshita, A. Leung, S. Simon, E. Evans, Long-lived, high-strength states of ICAM-1 bonds to beta(2) integrin, II: lifetimes of LFA-1 bonds under force in leukocyte signaling, Biophys. J. 98 (2010) 1467–1475.
[32] E. Evans, K. Kinoshita, Using force to probe single-molecule receptor-cytoskeletal anchoring beneath the surface of a living cell, Methods Cell Biol. 83 (2007) 373–396.
[33] C.S. Lopes, J. Curty, F.A. Carvalho, A. Hernandez-Machado, K. Kinoshita, N. C. Santos, R.D.M. Travasso, A mathematical model of fibrinogen-mediated erythrocyte-erythrocyte adhesion, Commun Biol 6 (2023) 192.
[34] E.A. Evans, R. Waugh, L. Melnik, Elastic area compressibility Modulus of red-cell membrane, Biophys. J. 16 (1976) 585–595.
[35] R. Waugh, E.A. Evans, Thermoelasticity of red blood cell membrane, Biophys. J. 26 (1979) 115–131.
[36] D.B. Min, J.M. Boff, Chemistry and reaction of singlet oxygen in foods, Compr. Rev. Food Sci. Food Saf. 1 (2002) 58–72.
[37] M.K. Kuimova, G. Yahioglu, P.R. Ogilby, Singlet oxygen in a cell: spatially dependent lifetimes and quenching rate constants, J. Am. Chem. Soc. 131 (2009) 332–340.
[38] J. Baier, M. Maier, R. Engl, M. Landthaler, W. Bäumler, Time-resolved investigations of singlet oxygen luminescence in water, in phosphatidylcholine, and in aqueous suspensions of phosphatidylcholine or HT29 cells, J. Phys. Chem. B 109 (2005) 3041–3046.
[39] S. Hackbarth, J. Schlothauer, A. Preuß, B. Röder, New insights to primary photodynamic effects – singlet oxygen kinetics in living cells, J. Photochem. Photobiol. B Biol. 98 (2010) 173–179.
[40] M.Y. Li, C.S. Cline, E.B. Koker, H.H. Carmichael, C.F. Chignell, P. Bilski, Quenching of singlet molecular oxygen (1O2) by azide anion in solvent mixtures, Photochem. Photobiol. 74 (2001) 760–764.
[41] H. Liu, P.J.H. Carter, A.C. Laan, R. Eelkema, A.G. Denkova, Singlet oxygen sensor green is not a suitable probe for (1)O(2) in the presence of ionizing radiation, Sci. Rep. 9 (2019) 8393.
[42] E.A. Evans, R.M. Hochmuth, Membrane viscoelasticity, Biophys. J. 16 (1976) 1–11.
[43] G. Ramdani, G. Langsley, ATP, an extracellular signaling molecule in red blood cells: a messenger for malaria? Biom. J. 37 (2014) 284–292.
[44] M.N. Moller, F. Orrico, S.F. Villar, A.C. Lopez, N. Silva, M. Donze, L. Thomson, A. Denicola, Oxidants and antioxidants in the redox biochemistry of human red blood cells, ACS Omega 8 (2023) 147–168.
[45] R.M. Hochmuth, C.A. Evans, H.C. Wiles, J.T. McCown, Mechanical measurement of red cell membrane thickness, Science 220 (1983) 101–102.
[46] S. Himbert, R.J. Alsop, M. Rose, L. Hertz, A. Dhaliwal, J.M. Moran-Mirabal, C. P. Verschoor, D.M.E. Bowdish, L. Kaestner, C. Wagner, M.C. Rheinstädter, The molecular structure of human red blood cell membranes from highly oriented, solid supported multi-lamellar membranes, Sci. Rep. 7 (2017) 39661 (EP).
[47] K.A. Riske, T.P. Sudbrack, N.L. Archilha, A.F. Uchoa, A.P. Schroder, C.M. Marques, M.S. Baptista, R. Itri, Giant vesicles under oxidative stress induced by a membrane-anchored photosensitizer, Biophys. J. 97 (2009) 1362–1370.
[48] G. Weber, T. Charitat, M.S. Baptista, A.F. Uchoa, C. Pavani, H.C. Junqueira, Y. Guo, V.A. Baulin, R. Itri, C.M. Marques, A.P. Schroder, Lipid oxidation induces structural changes in biomimetic membranes, Soft Matter 10 (2014) 4241–4247.
[49] P. Ways, D.J. Hanahan, Characterization and quantification of red cell lipids in normal man, J. Lipid Res. 5 (1964) 318–328.
[50] J.T. Dodge, G.B. Phillips, Composition of phospholipids and of phospholipid fatty acids and aldehydes in human red cells, J. Lipid Res. 8 (1967) 667–675.
[51] A.M. Timperio, C. Mirasole, A. D'Alessandro, L. Zolla, Red blood cell lipidomics analysis through HPLC-ESI-qTOF: application to red blood cell storage, J. Integr. Omics A Methodolog. 3 (2013) 11–24.
[52] G. Scanavachi, A. Coutinho, A.A. Fedorov, M. Prieto, A.M. Melo, R. Itri, Lipid hydroperoxide compromises the membrane structure organization and softens bending rigidity, Langmuir 37 (2021) 9952–9963.
[53] S.E. Lux, Anatomy of the red cell membrane skeleton: unanswered questions, Blood 127 (2016) 187–199.
[54] M. Salomao, X. Zhang, Y. Yang, S. Lee, J.H. Hartwig, J.A. Chasis, N. Mohandas, X. An, Protein 4.1R-dependent multiprotein complex: new insights into the structural organization of the red blood cell membrane, Proc. Natl. Acad. Sci. U. S. A. 105 (2008) 8026–8031.
[55] Y. Park, C.A. Best, T. Auth, N.S. Gov, S.A. Safran, G. Popescu, S. Suresh, M.S. Feld, Metabolic remodeling of the human red blood cell membrane, Proc. Natl. Acad. Sci. U. S. A. 107 (2010) 1289–1294.
[56] H. Li, Y. Zhang, V. Ha, G. Lykotrafitis, Modeling of band-3 protein diffusion in the normal and defective red blood cell membrane, Soft Matter 12 (2016) 3643–3653.
[57] T. Aoki, A comprehensive review of our current understanding of red blood cell (RBC) glycoproteins, Membranes (Basel) 7 (2017).
[58] W.A. Anong, T.L. Weis, P.S. Low, Rate of rupture and reattachment of the band 3-ankyrin bridge on the human erythrocyte membrane, J. Biol. Chem. 281 (2006) 22360–22366.
[59] C.C. Krieger, X. An, H.Y. Tang, N. Mohandas, D.W. Speicher, D.E. Discher, Cysteine shotgun-mass spectrometry (CS-MS) reveals dynamic sequence of protein structure changes within mutant and stressed cells, Proc. Natl. Acad. Sci. U. S. A. 108 (2011) 8269–8274.
[60] E. Ferru, K. Giger, A. Pantaleo, E. Campanella, J. Grey, K. Ritchie, R. Vono, F. Turrini, P.S. Low, Regulation of membrane-cytoskeletal interactions by tyrosine phosphorylation of erythrocyte band 3, Blood 117 (2011) 5998–6006.
[61] A. Pantaleo, E. Ferru, F. Carta, F. Mannu, L.F. Simula, A. Khadjavi, P. Pippia, F. Turrini, Irreversible AE1 tyrosine phosphorylation leads to membrane vesiculation in G6PD deficient red cells, PLoS One 6 (2011), e15847.
[62] H. Chu, M.M. McKenna, N.A. Krump, S. Zheng, L. Mendelsohn, S.L. Thein, L. J. Garrett, D.M. Bodine, P.S. Low, Reversible binding of hemoglobin to band 3 constitutes the molecular switch that mediates O2 regulation of erythrocyte properties, Blood 128 (2016) 2708–2716.
[63] H. Shimo, S.N. Arjunan, H. Machiyama, T. Nishino, M. Suematsu, H. Fujita, M. Tomita, K. Takahashi, Particle simulation of oxidation induced band 3 clustering in human erythrocytes, PLoS Comput. Biol. 11 (2015), e1004210.
[64] E.A. Nigg, R.J. Cherry, Anchorage of a band 3 population at the erythrocyte cytoplasmic membrane surface: protein rotational diffusion measurements, Proc. Natl. Acad. Sci. U. S. A. 77 (1980) 4702–4706.
[65] G.C. Kodippili, J. Spector, C. Sullivan, F.A. Kuypers, R. Labotka, P.G. Gallagher, K. Ritchie, P.S. Low, Imaging of the diffusion of single band 3 molecules on normal and mutant erythrocytes, Blood 113 (2009) 6237–6245.
[66] M.R. Deziel, A.W. Girotti, Photodynamic action of bilirubin on liposomes and erythrocyte membranes, J. Biol. Chem. 255 (1980) 8192–8198.
[67] M. Bancirova, Sodium azide as a specific quencher of singlet oxygen during chemiluminescent detection by luminol and Cypridina luciferin analogues, Luminescence 26 (2011) 685–688.
[68] S. Sankarapandi, J.L. Zweier, Evidence against the generation of free hydroxyl radicals from the interaction of copper,zinc-superoxide dismutase and hydrogen peroxide, J. Biol. Chem. 274 (1999) 34576–34583.
[69] B. Halliwell, J.M.C. Gutteridge, Role of free-radicals and catalytic metal-ions in human-disease - an overview, Methods Enzymol. 186 (1990) 1–85.
[70] M.S. Baptista, J. Cadet, P. Di Mascio, A.A. Ghogare, A. Greer, M.R. Hamblin, C. Lorente, S.C. Nunez, M.S. Ribeiro, A.H. Thomas, M. Vignoni, T.M. Yoshimura, Type I and type II photosensitized oxidation reactions: guidelines and mechanistic pathways, Photochem. Photobiol. 93 (2017) 912–919.
[71] E. Niki, Role of vitamin E as a lipid-soluble peroxyl radical scavenger: in vitro and in vivo evidence, Free Radic. Biol. Med. 66 (2014) 3–12.
[72] G. Aldini, A. Altomare, G. Baron, G. Vistoli, M. Carini, L. Borsani, F. Sergio, N-acetylcysteine as an antioxidant and disulphide breaking agent: the reasons why, Free Radic. Res. 52 (2018) 751–762.
[73] I. Morel, J. Cillard, G. Lescoat, O. Sergent, N. Pasdeloup, A.Z. Ocaktan, M. A. Abdallah, P. Brissot, P. Cillard, Antioxidant and free radical scavenging activities of the iron chelators pyoverdin and hydroxypyrid-4-ones in iron-loaded hepatocyte cultures: comparison of their mechanism of protection with that of desferrioxamine, Free Radic. Biol. Med. 13 (1992) 499–508.
[74] K. Fukuhara, I. Nakanishi, K. Imai, M. Mizuno, K.I. Matsumoto, A. Ohno, DTPA-bound planar Catechin with potent antioxidant activity triggered by Fe(3+) coordination, Antioxidants (Basel) 12 (2023).